

# Supramolecular Control in Nanostructured Film Architectures for Detecting Breast Cancer

Juliana Coatrini Soares,<sup>\*,†</sup> Flavio Makoto Shimizu,<sup>†</sup> Andrey Coatrini Soares,<sup>†</sup> Luciano Caseli,<sup>‡</sup> Jacqueline Ferreira,<sup>§</sup> and Osvaldo N. Oliveira, Jr.<sup>†</sup>

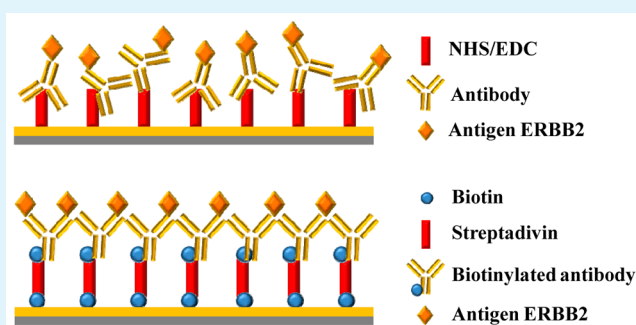
<sup>†</sup>São Carlos Institute of Physics, University of São Paulo, 369, 13560-970 São Carlos, São Paulo, Brazil

<sup>‡</sup>Institute of Environmental, Chemical and Pharmaceutical Sciences, Federal University of Sao Paulo, 09972-970 Diadema, São Paulo, Brazil

<sup>§</sup>Institute of Chemistry, Federal University of Rio Grande do Sul, 15003, 91501-970 Porto Alegre, Rio Grande do Sul, Brazil

**ABSTRACT:** The need for early detection of various diseases, including breast cancer, has motivated research into nanomaterials that can be assembled in organized films which serve as biosensors. Owing to the variety of possible materials and film architectures, procedures are required to design optimized biosensors. In this study, we combine surface-specific methods to monitor the assembly of antibodies on nanostructured films with two distinct architectures. In the first, a layer of the antibody type mouse anti-HER2 (clone tab250) was immobilized on a self-assembled monolayer (SAM) of 11-mercaptopundecanoic acid modified with *N*-hydroxysuccinimide (NHS) and 1-ethyl-3-(3-(dimethylamino)propyl)carbodiimide (EDC). In the second approach, a SAM of cysteamine was coated with a biotin/streptavidin bilayer on which a layer of biotinylated antibody type MSx2HUp185/her biotin was adsorbed. The rougher, less passivating coating with cysteamine determined from cyclic voltammetry and scanning electron microscopy led to biosensors that are more sensitive to detect the breast cancer ERBB2 (HER2) biomarker in impedance spectroscopy measurements. This higher distinguishing ability of the cysteamine-containing film architecture was proven with information visualization methods to treat the impedance data. Polarization-modulated infrared reflection absorption spectroscopy (PM-IRRAS) confirmed that biosensing resulted from the antibody–ERBB2 antigen affinity.

**KEYWORDS:** biosensors, breast cancer, nanostructured films, impedance spectroscopy, information visualization



## 1. INTRODUCTION

Breast cancer is among the most commonly diagnosed, accounting for ca. 12% of all cancer cases in the world, according to the International Agency for Research on Cancer (IARC).<sup>1</sup> Early diagnosis is crucial to enhance therapeutic effectiveness and prevent relapse by the patient,<sup>2</sup> which can be performed by detecting biomarkers<sup>3,4</sup> with biosensors such as those containing immobilized biomolecules in nanostructured films.<sup>3</sup> Biomarkers are typically detected in human fluids such as blood, serum, urine, or cerebral spinal fluid, but they can also be present in tumor cells.<sup>4</sup> For breast cancer, in particular, an important biomarker is the human epidermal growth factor receptor 2 (ERBB2 or HER2), expressed on the cell surface.<sup>3</sup> The measurement of ERBB2 concentration in tumor cells provides diagnostic, prognostic, and treatment information since a targeted therapeutic is available.<sup>5</sup> Monitoring ERBB2 levels is important because amplification or overexpression of the ERBB2 gene occurs in approximately 15–30% of breast cancers, in addition to being reported for ovarian, stomach, and aggressive forms of uterine cancer, such as uterine serous endometrial carcinoma.<sup>6–8</sup> Breast cancer patients, in particular,

have elevated ERBB2 concentrations (15–75 ng/mL) in their blood compared to those (2–15 ng/mL) observed for normal individuals.<sup>9</sup>

Various biosensors have been reported in the literature for detecting ERBB2 (HER2), employing mostly electrochemical methods. For instance, screen-printed carbon electrodes modified with gold nanoparticles and containing monoclonal antibodies were used to detect HER2 with a limit of detection (LOD) of 4.4 ng/mL.<sup>10</sup> In a similar approach, antibodies were attached to iron oxide nanoparticles, forming bioconjugates responsive to a wide range of HER2 concentrations.<sup>11</sup> With regard to other principles of detection applied to HER2, mention can be made of an aptasensor based on impedance spectroscopy<sup>9</sup> and an optofluidic ring resonator (OFRR).<sup>2</sup>

The performance of biosensors and/or immunosensors depends on the film architecture because they normally include nanomaterials and biomolecules,<sup>12</sup> in which synergy is sought

**Received:** February 10, 2015

**Accepted:** May 20, 2015

**Published:** May 20, 2015

in the properties of the different components. The three most used methods to assemble these nanostructured films are Langmuir–Blodgett (LB),<sup>13–16</sup> layer-by-layer (LbL),<sup>17</sup> and self-assembled monolayers (SAMs) techniques.<sup>18</sup> Important challenges are the control of film architecture in order to minimize denaturing of the biomolecules and enhance the sensitivity and selectivity. The choice of the biomolecules is another relevant issue, and systems based on antigen–antibody recognition elements provide fast detection<sup>4</sup> and accurate diagnosis.<sup>19</sup> The presence of the biomarker as analyte may be detected through different methods, using mostly optical and electrical principles,<sup>4</sup> including impedance spectroscopy used here.<sup>20</sup> Advantages of biosensors over other methods for detecting cancer cells are the possible cost reduction and real time detection.<sup>21</sup>

In this work we focus on the importance of film architectures for obtaining efficient immunosensors to detect ERBB2 to levels that are competitive with other immunosensors in the literature. Two ways to immobilize antibodies are tested, including direct immobilization by covalent attachment and immobilization in multiple steps by bioaffinity. In order to compare the film properties for the two architectures, we employ scanning electron microscopy (SEM), polarization-modulated infrared reflection absorption spectroscopy (PM-IRRAS), and contact angle measurements. ERBB2 detection was carried out with electrical impedance spectroscopy whose data were treated with information visualization methods,<sup>22</sup> which clearly demonstrate the distinction between samples containing different ERBB2 concentrations.

## 2. EXPERIMENTAL SECTION

**2.1. Modified Electrodes with Two Film Architectures.** For both film characterization and production of biosensing units, two distinct film architectures were used, which are represented in Figures 1 and 2. In the first architecture, referred to as MUA1, gold electrodes

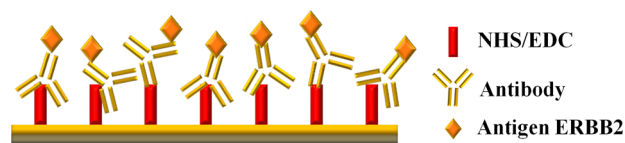


**Figure 1.** Film architecture referred to as MUA1, which contains a SAM of 11-mercaptoundecanoic acid (MUA) whose terminal groups were activated with NHS/EDC functionalization on which a layer of the type mouse anti-HER2 (clone tab250) antibody was immobilized. Also shown are the detected antigen ERBB2 molecules.

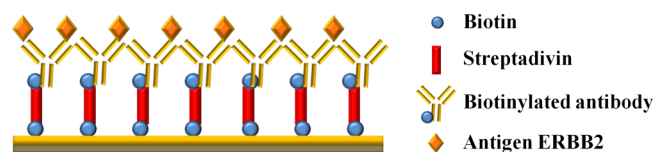


**Figure 2.** Film architecture referred to as Cyst1, in which the gold electrode was initially coated with a cysteamine SAM. Then, a bilayer of biotin/streptavidin was adsorbed, on which a layer of biotinylated antibody type MSx2HUp185/her was deposited. Also shown are detected molecules of the ERBB2 biomarker.

were initially coated with a thiol SAM of 11-mercaptoundecanoic acid (MUA) (Sigma-Aldrich, St. Louis, MO, USA) by immersing into a 1 mmol L<sup>-1</sup> solution for 48 h, and then washed with distilled water and ethanol to remove nonadsorbed molecules. In order to prepare for adsorption of antibodies, the acid terminal groups of this SAM were

activated by incubation into 0.1 mol L<sup>-1</sup> *N*-hydroxysuccinimide (NHS; Sigma-Aldrich) and 0.1 mol L<sup>-1</sup> 1-ethyl-3-(3-(dimethylamino)propyl)-carbodiimide (EDC; Sigma-Aldrich) for 24 h. The NHS–EDC interaction between thiol molecules allows for the adsorption of a layer of the antibody type mouse anti-HER2 (clone tab250; Invitrogen, Carlsbad, CA, USA).

For the film architecture shown in Figure 2, referred to as Cyst1, a SAM monolayer of cysteamine (Sigma-Aldrich) was prepared with the same procedures as given previously, but with a 6 mmol L<sup>-1</sup> ethanol solution for periods of 1, 48, and 72 h. The amino terminal groups of cysteamine SAMs allow for covalent binding of any modified protein with NHS groups. The sample containing cysteamine SAM was immersed in an 18 mmol L<sup>-1</sup> solution of biotin (Sigma-Aldrich) modified with NHS groups (BNHS) in dimethyl sulfoxide (DMSO; Sigma-Aldrich) for 3 h, with biotin–NHS binding to cysteamine via the amine group. The film with biotin monolayer atop was then immersed in a 0.25 mg/mL streptavidin solution (Sigma-Aldrich) in PBS for 1 h. The highly specific interaction between streptavidin and biotin was exploited to adsorb a layer of the biotinylated antibody type MSx2HUp185/her (Invitrogen). It is worth mentioning that a matrix with a protein such as bovine serum albumin (BSA) was not necessary in this work because MUA1 and Cyst1 architectures were already sufficient to detect ERBB2 (HER2) antigen owing to the antibody–antigen specific interaction. Obviously, if the blocking during the SAM deposition is performed, detection may be optimized, but in subsidiary experiments in which BSA was added we did not notice significant changes in the electrical response, probably because the specific interactions were not affected.

**2.2. Film Characterization.** Cysteamine/biotin/streptavidin (Cyst1) and MUA/NHS/EDC (MUA1) films were characterized by cyclic voltammetry in a 3-electrode electrochemical cell using a Dropsens Micropotentiostat (Dropsens, Oviedo, Spain). The working electrode with 4 mm diameter and the counter electrode were made of gold, whereas the reference electrode and electric contacts were made of silver. A sweep potential was applied between  $-0.1$  and  $0.6$  V vs Ag/AgCl, at a scan rate of  $50$  mV s<sup>-1</sup> in an aqueous solution of 1 mmol L<sup>-1</sup> K<sub>4</sub>[Fe(CN)<sub>6</sub>] (Synth, Diadema, Brazil) and KCl 0.1 mmol L<sup>-1</sup> (Synth). The morphology of these films was assessed with scanning electron microscopy (SEM) images acquired in a FEI Magellan 400 L (FEI, Hillsboro, OR, USA) and Phillips XL 30 FEG (Phillips, Eindhoven, The Netherlands). The samples were fixed with double-sided tape on Al supports covered with a ca. 20 nm thick Au layer, in a vacuum chamber to remove moisture, and positioned on the sample holder. All of the substrates were cleaned according to previously described procedures.<sup>23</sup>

Surface-specific techniques were also used in monitoring film growth. PM-IRRAS measurements were performed using a KSV PMI 550 Instrument (KSV Instruments, Helsinki, Finland) with spectral resolution of 8 cm<sup>-1</sup> and an incidence angle of 80°. The films used as biosensors were characterized with contact angle measurements using the sessile drop technique for determining surface energy, dispersion, and polar components. Deionized water and diiodomethane were the liquids employed. A CAM 100 goniometer from KSV Instruments was used to measure contact angles, with which the surface energy was calculated with the Owens and Wendt method, according to eq 1.<sup>24</sup>

$$\gamma_L(1 + \cos(\theta)) = 2(\sqrt{\gamma_L^D \gamma_S^D} + \sqrt{\gamma_L^P \gamma_S^P}) \quad (1)$$

where  $\gamma_L$  is the liquid surface tension,  $\theta$  is the angle between the solid and liquid interface,  $\gamma_L^D$ ,  $\gamma_S^D$ ,  $\gamma_L^P$ , and  $\gamma_S^P$  are polar (P) and dispersive (D) components of solid and liquid surface tensions.

**2.3. Detection with Impedance Measurements.** Electrical impedance measurements were carried out with a Solartron 1260A impedance/gain phase analyzer (Solartron, Farnborough, England) in the range from 1 to 10<sup>6</sup> Hz. The units sensing were produced by depositing films according to the architectures depicted in Figures 1 and 2 onto 50 pairs of gold interdigitated electrodes, 10  $\mu$ m wide and 10  $\mu$ m apart from each other. These interdigitated electrodes were designed to exhibit a capacitive profile, being fabricated by photolithography at the Brazilian Nanotechnology National Labo-

ratory (LNNano-LNLS). BK7 glass slides were coated with hexamethyldisiloxane (HMDS; Sigma-Aldrich) and AZ 4210 photoresist (Shipley, Marlborough, MA, USA), and then the gold tracks were deposited by sputtering.

**2.4. Data Treatment with Information Visualization Methods.** The capacitance values obtained from impedance measurements were statistically analyzed using a free software suite referred to as Projection Explorer Sensors (Pex-Sensors)<sup>25</sup> which contains several projection techniques such as interactive document mapping (IDMAP) and the multidimensional data visualization parallel coordinates (PC). IDMAP uses Euclidean distance to convey dissimilarity in the set of capacitance values  $X = \{x_1, x_2, \dots, x_n\}$  obtained with one or more sensing units for different frequencies. The dissimilarity between two data instances  $i$  and  $j$  is given by  $\delta(x_i, x_j)$ . These data are projected onto a lower dimension space, with  $Y = \{y_1, y_2, \dots, y_n\}$  representing the positioning of the visual elements, where  $d(y_i, y_j)$  is the distance function on the projected space. The projection technique employs a function  $f: X \rightarrow Y$  that attempts to minimize  $|\delta(x_i, x_j) - d(f(x_i), f(x_j))| \forall x_i, x_j \in X$ . The function minimized in IDMAP is

$$S_{\text{IDMAP}} = \frac{\delta(x_i, x_j) - \delta_{\min}}{\delta_{\max} - \delta_{\min}} - d(y_i, y_j) \quad (2)$$

where  $\delta_{\min}$  and  $\delta_{\max}$  are the minimum and maximum distances between data instances.

The parallel coordinates technique departs from the conventional approach of mapping attributes to orthogonal coordinate axes of a Cartesian plane, by mapping the set of data instances as equally spaced parallel axes that are scaled to depict the range of measured values. For capacitance vs frequency measurements considered here, the capacitance measured with the sensing units are mapped as polyines by intersecting the axes on the points representing the value measured, where each axis represents a specific frequency. This visual representation is effective to reveal data distributions and correlation among attributes.<sup>26,27</sup>

### 3. RESULTS AND DISCUSSION

#### 3.1. Monitoring the Fabrication of Film Architectures.

The design of film architectures for enhanced sensing based on biorecognition events must fulfill several requirements, some of which may conflict with each other. For instance, in electrochemical biosensors full electrode passivation obtained with homogeneous coating may be advantageous in order to avoid false positives. In biosensing using impedance spectroscopy as the principle of detection, on the other hand, heterogeneous coating with less passivation may generate larger surface areas, thus leading to higher sensitivity. For the two architectures tested in the present work, a more complete electrode coverage occurred for the MUA1 multilayer film, as described later.

Electrode passivation was determined using cyclic voltammetry and monitoring the  $[\text{Fe}(\text{CN})_6]^{3-}/[\text{Fe}(\text{CN})_6]^{4-}$  redox process, which exhibits anodic and cathodic peaks at 0.25 and 0.1 V, respectively.<sup>28,29</sup> Full passivation of the Au electrode was observed with adsorption of thiol groups from MUA, as indicated with the almost entire extinction of the redox process of  $\text{K}_4[\text{Fe}(\text{CN})_6]$  in Figure 3. Coverage with the SAM of MUA prevented diffusion of electroactive species toward the gold surface. In contrast, passivation was only partial even after 72 h of adsorption of cysteamine, as seen in the increased oxidation and reduction peaks in Figure 4. The incomplete coverage may be attributed to the small van der Waals forces operating between short chains of cysteamine.<sup>29</sup> In addition, the cysteamine layer increases reversibility of  $[\text{Fe}(\text{CN})_6]^{3-}/[\text{Fe}(\text{CN})_6]^{4-}$  and increased redox peak currents in comparison with the Au surface owing to catalysis of negatively charged

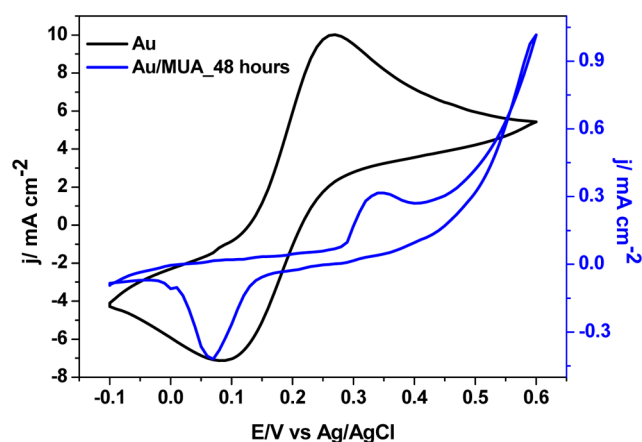


**Figure 3.** Cyclic voltammograms for 0.001 mol L<sup>-1</sup> K<sub>4</sub>[Fe(CN)<sub>6</sub>], 0.1 mol L<sup>-1</sup> KCl, a scan rate of 50 mV·s<sup>-1</sup>, between -0.1 and 0.6 V vs Ag/AgCl, for the Au/MUA electrode, with MUA adsorption during 48 h.

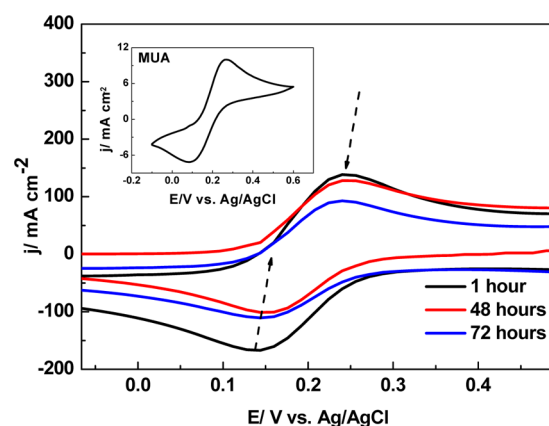


**Figure 4.** Cyclic voltammograms for 0.001 mol L<sup>-1</sup> K<sub>4</sub>[Fe(CN)<sub>6</sub>], 0.1 mol L<sup>-1</sup> KCl, a scan rate of 50 mV·s<sup>-1</sup>, between -0.1 and 0.6 V vs Ag/AgCl for the Au/cysteamine electrode, where adsorption times for cysteamine varied from 1 to 72 h. The inset shows the voltammogram for bare gold.

$[\text{Fe}(\text{CN})_6]^{3-}/4-$  by the positively charged primary amine headgroup of the cysteamine electrode.<sup>30</sup>

The extent of electrode coverage for the MUA and cysteamine SAMs, inferred from the cyclic voltammetry results, is corroborated with the analysis of SEM images in Figure 5. Aggregates made of cysteamine, which has only two methylene groups, appear distributed heterogeneously on the gold surface in Figure 5a, consistent with the expectation of poorly organized SAMs made with alkanethiols possessing less than nine methylene groups.<sup>31</sup> The cysteamine films coated with a biotin monolayer in Figure 5b and then a streptavidin monolayer in Figure 5c are also irregular, exhibiting large aggregates. Parts d and e of Figure 5 show much more homogeneous coverage of the gold electrode for a MUA SAM and MUA/NHS/EDC films, respectively, again consistent with the cyclic voltammetry results.

The cyclic voltammetry and SEM preceding results showed effects from film adsorption, but they cannot be used to confirm the idealized architectures in Figures 1 and 2. This was done here by monitoring film formation, step by step, with PM-IRRAS, which allows for identifying adsorbed functional groups. With the setup used, the positive bands indicate the vibration moment parallel to the electrode plane, while negative

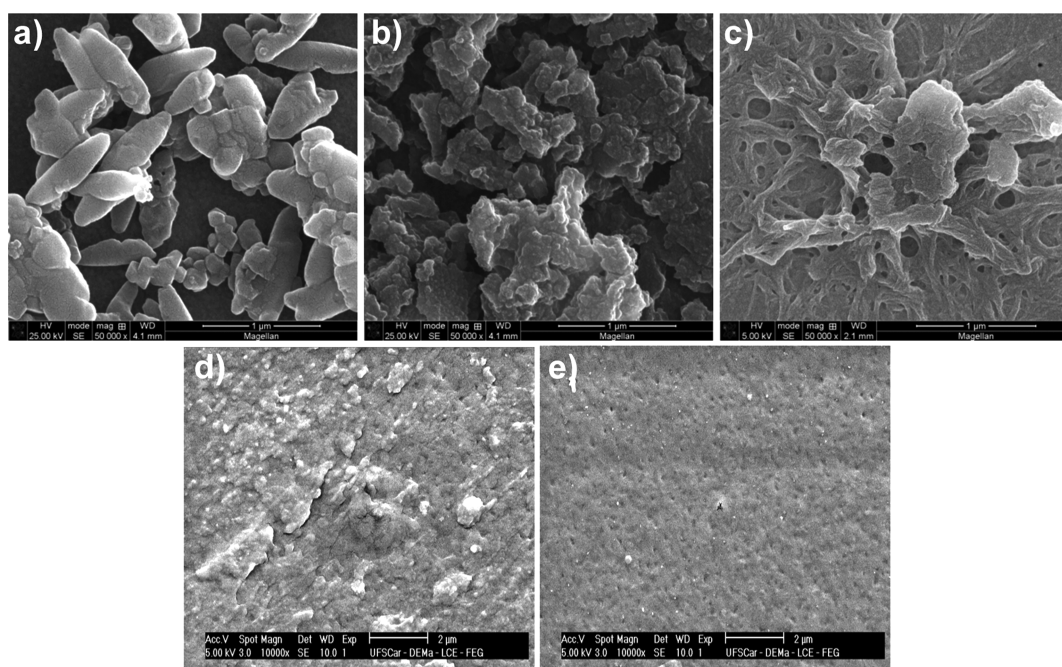


**Figure 5.** SEM images of the gold surface modified with cysteamine (a), cysteamine/biotin (b), cysteamine/biotin–streptavidin (c), MUA (d), and MUA/NHS/EDC (e).

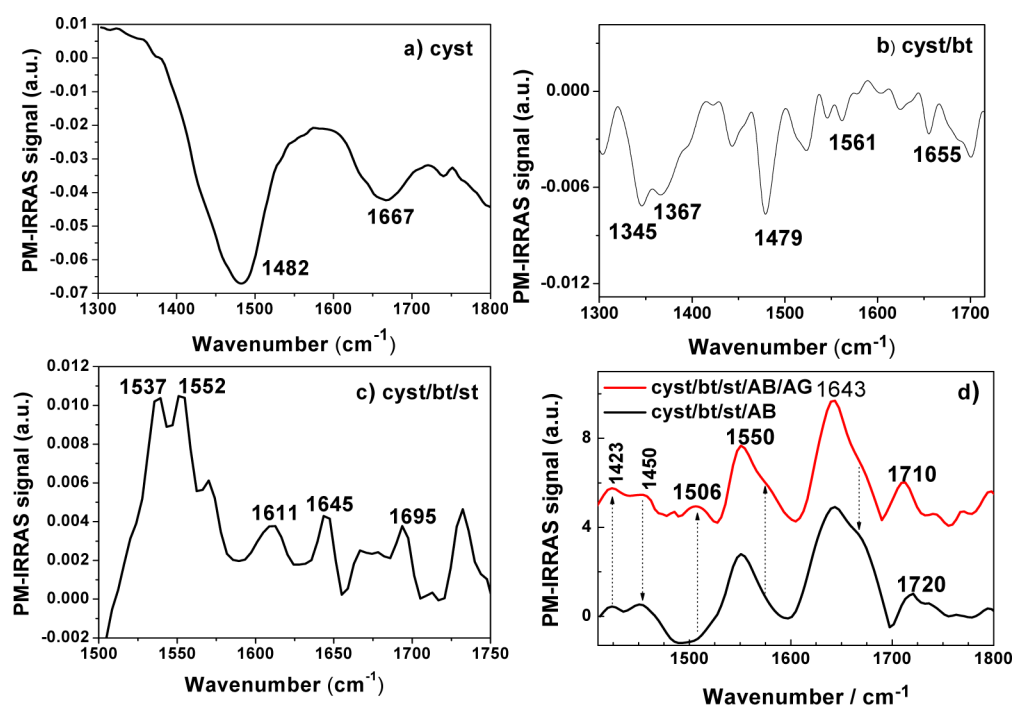


**Figure 6.** PM-IRRAS spectra of the films containing a monolayer of cyst (a), cyst/bt (b), cyst/bt/st (c), and cyst/bt/st/AB and cyst/bt/st/AB/AG (d) adsorbed onto Au substrate.

bands are indicative of perpendicular orientation. Figure 6 shows the spectra for the cysteamine-containing film corresponding to the architecture in Figure 2. The formation of a cysteamine SAM (cyst) on gold is illustrated in Figure 6a, featuring thiol NH stretch and CH<sub>2</sub> deformation bands at 1667 and 1482 cm<sup>-1</sup>, respectively.<sup>32</sup> Adsorption of a biotin monolayer (cyst/bt) brings the bands in Figure 6b, at 1655 and 1561 cm<sup>-1</sup>, assigned to C=O stretching and C–N bending mode from amides, respectively,<sup>33</sup> and bands at 1367

and 1345 cm<sup>-1</sup>, assigned to COO<sup>-</sup> symmetric stretching from carboxylic groups. As streptavidin is linked to biotin (cyst/bt/st), more discernible bands appear in Figure 6c due to amide I (C=O stretch) at the 1600–1700 cm<sup>-1</sup> region, which are related to secondary structures in polypeptides. The band at 1611 cm<sup>-1</sup> can be assigned to  $\beta$ -sheets, and those at 1645 and 1695 cm<sup>-1</sup> are assigned to unordered secondary structures and antiparallel  $\beta$ -sheets, respectively.<sup>34</sup> Amide II bands are seen at 1552 and 1537 cm<sup>-1</sup>, being attributed to CN and NH bending,

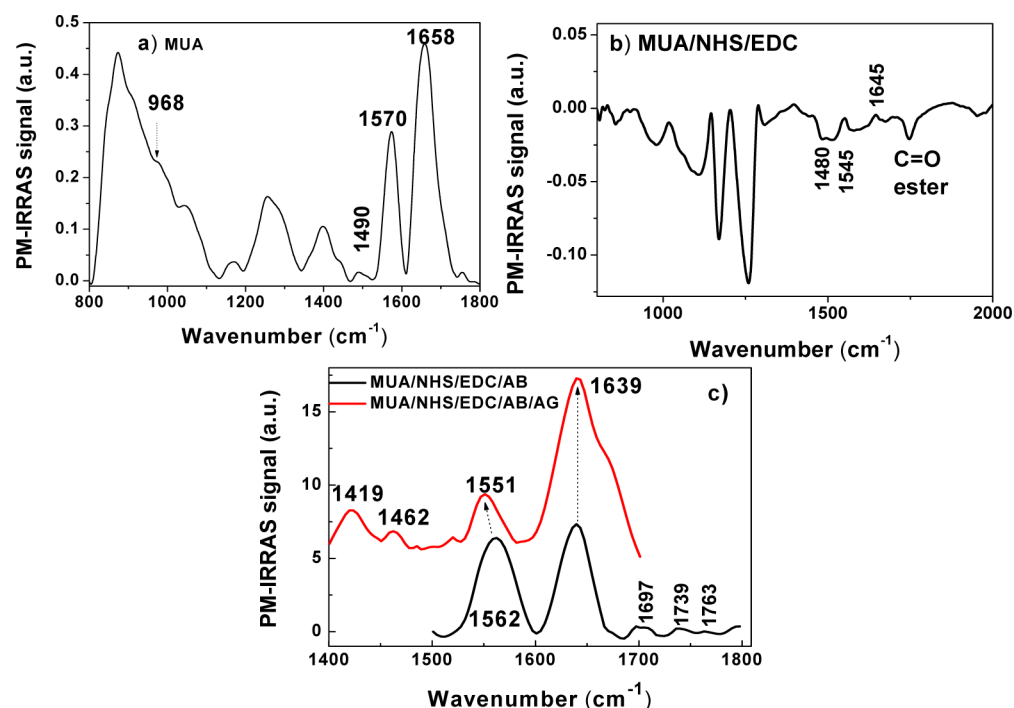


**Figure 7.** PM-IRRAS spectra of the film architecture containing MUA SAM (a), MUA/NHS/EDC (b), and MUA/NHS/EDC/AB and MUA/NHS/EDC/AB/AG (c) adsorbed onto Au substrate.

**Table 1. Contact Angle, Surface Energy, and Roughness of the Cyst1 and MUA1 Films Containing Water and Diiodomethane<sup>a</sup>**

	contact angle		surface energy (mJ m <sup>-2</sup> )	roughness RMS (nm)
	water	diiodomethane		
cyst	73	37	43.5	5.02
cyst/biotin/streptavidin	40	31	66.0	4.02
cyst/biotin/streptavidin/AB	51	34	59.2	17.08
cyst/biotin/streptavidin/AB/AG	26	36	71.8	7.84
MUA	32	40	63.2	3.08
MUA/NHS/EDC	42	31	64.9	2.07
MUA/NHS/EDC/AB	53	33	58.3	4.34
MUA/NHS/EDC/AB/AG	17	24	71.8	1.97

<sup>a</sup>AB refers to antibodies, and AG refers to antigen molecules.

respectively.<sup>31</sup> These results demonstrate specific binding of streptavidin to biotin.<sup>35</sup>

Deposition of a layer of antibodies (AB) yields an amide I band at 1643 cm<sup>-1</sup> which dominates the region between 1600 and 1700 cm<sup>-1</sup> in Figure 6d. Bands assigned to secondary structures appear only as shoulders, such as those at ca. 1680 cm<sup>-1</sup>. The ratio between the areas below the bands for amide I (~1600–1700 cm<sup>-1</sup>) and amide II (~1500–1600 cm<sup>-1</sup>) changed upon adsorption of AB, from 0.3 to 1.4 according to Figure 6c,d. Since a higher ratio is related to protein structuring, either the immobilized AB is more structured than biotin or AB induces ordering in biotin. With adsorption of an AG layer, this ratio remains close to 1.4 and bands at ~1710–1720 (C=O stretching in carboxylic acids) and 1423 and 1450 cm<sup>-1</sup> (C–H bending) are kept in Figure 6d. The major difference caused by AG adsorption is the appearance of a band at 1506 cm<sup>-1</sup>, assigned to C–N bending or benzene ring in aromatic compounds (in amino acid residues present in AG structures). This band can be either due to structuring of AG or induced order in AB owing to antigen–antibody interactions.<sup>35</sup>

The adsorption of multiple layers in the film architecture of Figure 1 was also confirmed with the PM-IRRAS spectra in Figure 7. The formation of a MUA SAM on gold is denoted by bands assigned to 11-mercaptopundecanoic acid, at 1658 cm<sup>-1</sup> (COO<sup>-</sup> antisymmetric stretch), 1490 and 1405 cm<sup>-1</sup> for CH<sub>2</sub> bending, and 1260 cm<sup>-1</sup> for COO<sup>-</sup> asymmetric stretch. The band at 1570 cm<sup>-1</sup> can be assigned to HOH bending in residual water.<sup>35</sup> With adsorption of NHS/EDC, Figure 7b shows bands due to the C=O group in 11-mercaptopundecanoic acid at 1740–1750 cm<sup>-1</sup>. The amide I band appears at 1645 cm<sup>-1</sup>, while the amide II band is at 1545 cm<sup>-1</sup>.<sup>30</sup> The band at 1263 cm<sup>-1</sup> is due to C–N in aromatic compounds. All of these bands are due to NHS, since the main bands for EDC do not appear in this spectral region. Adsorption of an AB layer yields an amide I band at 1639 cm<sup>-1</sup> and an amide II band at 1562 cm<sup>-1</sup>. When a layer of AG is adsorbed, the amide II band is shifted to 1551 cm<sup>-1</sup>, and the ratio between the areas below the amide I and amide II bands increases from 1.1 to 3.1.

The antibody–antigen interaction brought larger changes for the film architecture MUA1 than for the film architecture Cyst1, which is inferred by comparing Figures 6d and 7c. Of

special relevance is the change in the ratio between the areas below amide I and amide II bands induced by adsorption of a layer of AG, observed for MUA1 but not for Cyst1. Therefore, it seems that the more uniform coverage of the substrate afforded by MUA molecules, as indicated by cyclic voltammetry and SEM techniques, leads to stronger overall antibody–antigen interactions.

The surface energy of the nanostructured films, obtained from contact angle measurements with water and diiodomethane, was also affected by deposition of multiple layers in both film architectures MUA1 and Cyst1, as indicated in Table 1. Adsorption of a layer of antibodies (AB) reduced the surface energy, increased the surface roughness, and made the film less hydrophilic. This applied to both the films containing the biotin/streptavidin pair and those made with NHS/EDC. In contrast, adsorption of a layer of antigens (AG) made the films considerably more hydrophilic, with higher surface energy but with lower roughness, for both types of films, which means a stronger coverage of active sites of AB with the AG. A slightly higher difference in surface energy was measured for adsorption of AG on the MUA1 architecture, compared to the Cyst1 architecture, which is probably owing to the more extensive coverage of the substrate as inferred from the other results (cyclic voltammetry, SEM images, and PM-IRRAS spectra). These observations are relevant for biosensing because the sensitivity tends to increase with a higher number of active sites available on rough surfaces.

### 3.2. Detection of the ERBB2 Antigen Biomarker.

Detection of the ERBB2 antigen biomarker diluted in PBS solution was performed with electrical impedance spectroscopy measurements, where the sensing units were made with the nanostructured films according to the architectures depicted in Figures 1 and 2, deposited on interdigitated gold electrodes. The specific antibody–antigen interactions are sufficiently strong to yield measurable differences in the relative capacitance that is the difference between the capacitance response with and without antigen in solution vs frequency curves for all ERBB2 concentrations used, as indicated in Figure 8. Interestingly, for the Cyst1 film architecture in Figure 8b, significant differences were also observed at high frequencies, which is not typical of the response for sensing units made with nanostructured films. According to Taylor and Macdonald,<sup>36</sup> the electrical response of organic films in contact with an electrolyte is governed by different types of mechanisms depending on the frequency of the applied ac signal. At low frequencies, the response is dominated by double layer effects, which tend to be the most important frequency region for distinguishing similar liquid samples.<sup>11</sup> At intermediate frequencies (1–10 kHz), film properties prevail, whereas at higher frequencies (100 kHz and above) the most important contribution comes from the electrode geometry capacitance. Therefore, the ability to distinguish the various ERBB2 concentrations even at high frequencies for the Cyst1 sensor appears to indicate strong adsorption of ERBB2, which is indeed expected (as discussed later on). Nevertheless, a visual inspection points to a higher distinguishing ability at lower frequencies for both film architectures since capacitance is strongly affected by changes in the electrical double layer, which is also expected to be altered by adsorption.

Since one of the objectives in this study was to compare the two film architectures for biosensing, we used a multidimensional projection technique, referred to as IDMAP, to project the capacitance data shown in Figure 8 on 2D plots. In such

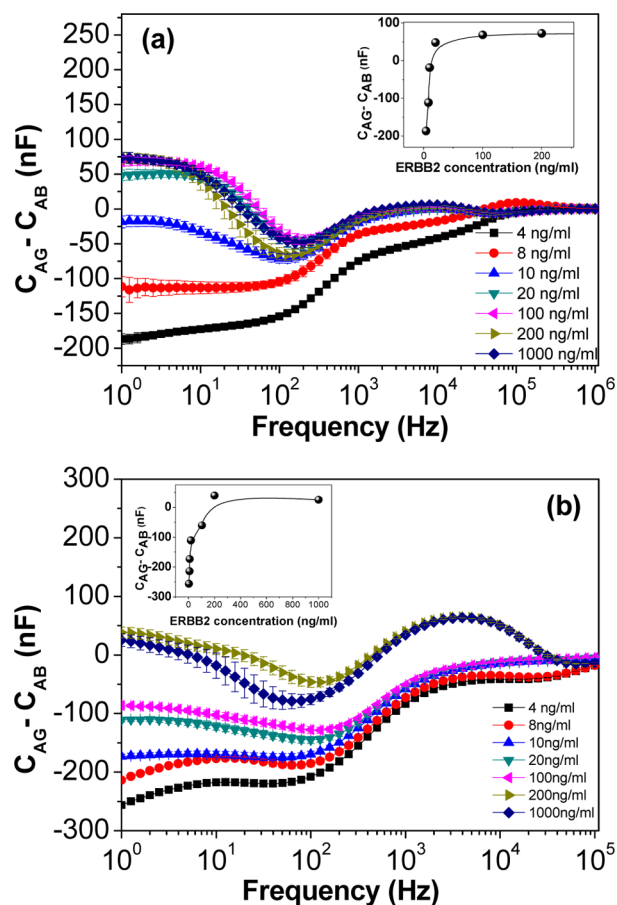


**Figure 8.** Relative capacitance ( $C_{AG} - C_{AB}$ ) vs. frequency spectra for (a) MUA1 and (b) Cyst1 electrodes immersed in PBS solutions with different ERBB2 concentrations. The insets show the changes in relative capacitance (nF) versus ERBB2 concentration at 1 Hz, with sharp increases at low concentrations before saturation occurs, as is typical of immunosensors based on antigen–antibody interactions.

projection, each capacitance spectrum is represented by a graphical marker, while the use of IDMAP is intended to preserve the similarity relationship in the original multidimensional space. That is to say, similar capacitance vs frequency curves should be projected close to each other on the 2D plots in Figure 9. IDMAP was chosen as the projection technique because it has been proven effective for treating biosensing data in several cases.<sup>26</sup> A comparison of the plots for the two film architectures in Figure 9 indicates that better distinction among the various concentrations of ERBB2 is obtained with the Cyst1 biosensor. Hence, the sensing performance in the present case appears to depend to a larger extent on the large surface area of the uneven film coverage for the Cyst1 architecture than on the more extensive coverage observed for the MUA1 architecture.

We also plotted the capacitance data with the parallel coordinates technique, which again indicates the higher ability of distinction of the Cyst1 biosensor. This can be done quantitatively by considering the silhouette coefficients value  $S$ , represented by colors on the top of the plots in Figures 10 and 11, calculated with eq 3.

$$S = \frac{1}{n} \sum_{i=1}^n \frac{(b_i - a_i)}{\max(a_i, b_i)} \quad (3)$$

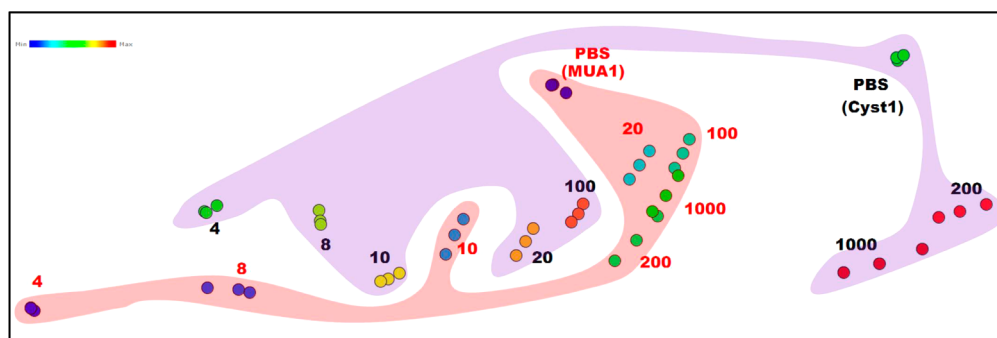


**Figure 9.** IDMAP plot for the capacitance data from MUA1 and Cyst1 electrodes for different ERBB2 concentrations (ng/mL).

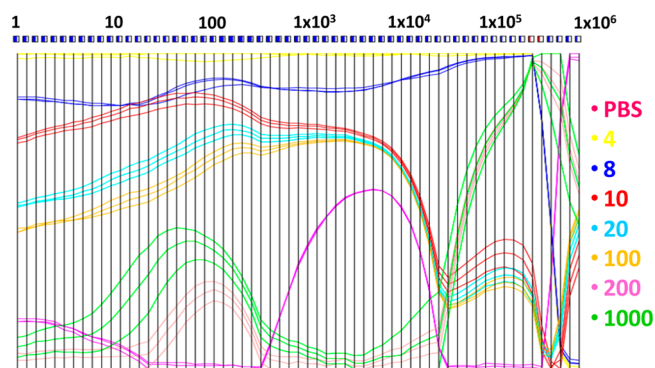


**Figure 10.** Parallel coordinates plot obtained from capacitance data measured with Cyst1 electrodes in different ERBB2 concentrations. The abscissa corresponds to the frequency while the ordinate brings normalized values of capacitance. A large number of blue boxes indicate that many frequencies are suitable for distinguishing among the different samples, represented by different colors, i.e., they had high silhouette coefficients. One may also note visually that distinction of the different samples is more effective at low frequencies.

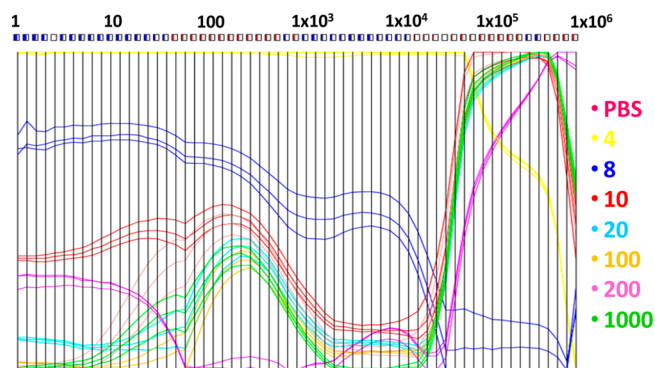


**Figure 11.** Parallel coordinates plot for the capacitance data measured with MUA1 electrodes for different ERBB2 concentrations. The abscissa corresponds to the frequency. The relatively large number of red boxes indicates that only a few frequencies are suitable for distinguishing among the samples. Note that the blue boxes are mostly located at low frequencies owing to effects on the double layer.

where  $a_i$  is the average of the calculated distances between the frequency curve of the  $i$ th sample and the curves of all of the samples with the same concentration as  $i$ ,  $b_i$  is the minimum distance between the frequency curve of the  $i$ th sample and the curves of all of the other samples with different concentrations from  $i$ , and  $n$  is the total number of samples.<sup>26,27,37</sup> The silhouette coefficient varies between  $-1$  and  $1$ ; blue boxes are indicative of frequency values for which distinction of the

samples is efficient, thus exhibiting positive  $S$  values up to  $1$ , whereas the frequencies marked as red boxes are not helpful to distinguish the various curves, taking negative  $S$  values down to  $-1$ .

For Cyst1 film the average silhouette coefficient for the 61 frequencies used is  $0.85$ . Such a high value reflects the large number of blue boxes in Figure 10, which are associated with frequencies that are useful for distinguishing among the different samples (represented by different colors). In contrast, the number of blue boxes is considerably smaller for the MUA1 biosensor, thus resulting in a lower average silhouette coefficient of  $0.68$ . Distinction is more efficient at low frequencies for which there are more blue boxes, for Cyst1 and MUA1, as already inferred from the visual inspection of Figure 8.

The conclusion from the statistical analysis of capacitance data that Cyst1 architecture is more efficient for ERBB2 detection than MUA1 architecture seems contradictory with the results from PM-IRRAS. In the latter, we found that the antigen–antibody interaction was stronger for MUA1. However, one should consider that the surface area of the Cyst1 sensing unit was larger owing to its rougher surface, as indicated by the results of surface characterization in Table 1. Moreover, double layer effects should predominate since the most significant changes in capacitance were observed at low frequencies.

The sensitivity of the two biosensors can be estimated from the concentration dependence of the change in relative capacitance in the insets of Figure 8 and from the IDMAP plots in Figure 9. It is clear that ERBB2 concentrations at the  $4$  ng/mL range or even lower can be detected. We used the capacitance values at a fixed frequency of  $1$  Hz in the concentration range between  $4$  and  $20$  ng/mL to obtain the calibration curve. The limit of detection (LOD) determined using the IUPAC method was  $0.88$  ng/mL for Cyst1 film and  $1.64$  ng/mL for MUA1 film. This level of sensitivity is comparable to the immunosensors reported in the literature for ERBB2,<sup>10,11,38</sup> though the comparison is not always fair because in some works real samples from blood serum were used, rather than the synthetic samples employed here. In any case, a LOD within a few nanograms per milliliter is already sufficient for early detection of breast cancer for which the threshold value is  $15$  ng/mL.

#### 4. CONCLUSION

Film architectures with two distinct ways to immobilize the antibody anti-HER2 were produced, where immobilization was either direct with covalent attachment or in multiple steps by

bioaffinity. These films were employed to detect ERBB2 antigen down to a few nanograms per milliliter using impedance spectroscopy, with the film architecture containing cysteamine in the bioaffinity attachment being more efficient. The higher sensitivity for this sensing unit was ascribed to the rougher, less passivating coating with cysteamine compared to the architecture containing MUA, as indicated by cyclic voltammetry and scanning electron microscopy images. The mechanism behind sensing is mostly associated with adsorption of the ERBB2 antigen onto its corresponding antibody, which was confirmed with the changes in amide bands in PM-IRRAS spectra. The detailed comparison between film architectures and performance in biosensing was made possible with surface-specific characterization methods, viz., PM-IRRAS spectroscopy and contact angle measurements, and information visualization methods through which the impedance spectroscopy data were analyzed. Because these methods are generic, the approach employed in this work can be extended to any other type of biosensor and indeed any device comprising sophisticated, complex supramolecular architectures.

## AUTHOR INFORMATION

### Corresponding Author

\*E-mail: julianacoatrini@gmail.com.

### Notes

The authors declare no competing financial interest.

## ACKNOWLEDGMENTS

We thank the FAPESP, CNPq, CAPES, and nBioNet network for financial support. Acknowledgments are also given to Angelo L. Gobbi and Maria H. O. Piazzetta for use of the microfabrication laboratory (LMF/LNNano-LNLS).

## REFERENCES

- (1) International Agency for Research on Cancer, <http://www.iarc.fr/> (accessed on Dec. 9, 2014).
- (2) Gohring, J. T.; Dale, P. S.; Fan, X. Detection of HER2 Breast Cancer Biomarker Using the Opto-Fluidic Ring Resonator Biosensor. *Sens. Actuators, B* **2010**, *146*, 226–230.
- (3) Chambers, J. P.; Arulanandam, B. P.; Matta, L. L.; Weis, A.; Valdes, J. J. Biosensor Recognition Elements. *Curr. Issues Mol. Biol.* **2008**, *10*, 1–12.
- (4) Bohunicky, B.; Mousa, S. S. Biosensors: The New Wave in Cancer Diagnosis. *Nanotechnol. Sci. Appl.* **2011**, *4*, 1–10.
- (5) Cole, K. D.; He, H. J.; Wang, L. Breast Cancer Biomarker Measurements and Standards. *Proteomics: Clin. Appl.* **2013**, *7*, 17–29.
- (6) Diaconu, I.; Cristea, C.; Harceaga, V.; Marrazza, G.; Berindan-Neagoe, I.; Sandulescu, R. Electrochemical Immunosensors in Breast and Ovarian Cancer. *Clin. Chim. Acta* **2013**, *425*, 128–138.
- (7) Slamon, D. J.; Godolphin, W.; Jones, L. A.; Holt, J. A.; Wong, S. J.; Keith, D. E.; Levin, W. J.; Stuart, S. G.; Udove, J.; Ullrich, A. Studies of the HER-2/Neu Proto-Oncogene in Human Breast and Ovarian Cancer. *Science* **1989**, *244*, 707–712.
- (8) Hung, M.-C.; Matin, A.; Zhang, Y.; Xing, X.; Sorgi, F.; Huang, L.; Yu, D. HER-2/Neu-Targeting Gene Therapy—A Review. *Gene* **1995**, *159*, 65–71.
- (9) Chun, L.; Kim, S. E.; Cho, M.; Choe, W. S.; Nam, J.; Lee, D. W.; Lee, Y. Electrochemical Detection of HER2 Using Single Stranded DNA Aptamer Modified Gold Nanoparticles Electrode. *Sens. Actuators, B* **2013**, *186*, 446–450.
- (10) Marques, R. C.; Viswanathan, S.; Nouws, H. P.; Delerue-Matos, C.; Gonzalez-Garcia, M. B. Electrochemical Immunosensor for the Analysis of the Breast Cancer Biomarker HER2 ECD. *Talanta* **2014**, *129*, 594–599.
- (11) Emami, M.; Shamsipur, M.; Saber, R.; Irajirad, R. An Electrochemical Immunosensor for Detection of a Breast Cancer Biomarker Based on Antiher2–Iron Oxide Nanoparticle Bioconjugates. *Analyst* **2014**, *139*, 2858–2866.
- (12) Oliveira, O. N., Jr.; Iost, R. M.; Siqueira, J. R., Jr.; Crespilho, F. N.; Caseli, L. Nanomaterials for Diagnosis: Challenges and Applications in Smart Devices Based on Molecular Recognition. *ACS Appl. Mater. Interfaces* **2014**, *6*, 14745–14766.
- (13) Zhang, A.; Hou, Y.; Jaffrezic-Renault, N.; Wan, J.; Soldatkin, A.; Chovelon, J. M. Mixed Urease/Amphiphile LB Films and Their Application for Biosensor Development. *Bioelectrochemistry* **2002**, *56*, 157–158.
- (14) Berzina, T. S.; Piras, L.; Troitsky, V. I. Study of Horseradish Peroxidase Activity in Alternate-Layer Langmuir Blodgett Films. *Thin Solid Films* **1998**, *327–329*, 621–626.
- (15) Godoy, S.; Violot, S.; Boullanger, P.; Bouchu, N.-N.; Leca-Bouvier, B. D.; Blum, L. J.; Girard-Egrot, A. P. Kinetics Study of Bungarus Fasciatus Venom Acetylcholinesterase Immobilised on a Langmuir-Blodgett Proteo-Glycolipidic Bilayer. *ChemBioChem* **2005**, *6*, 395–404.
- (16) Godoy, S.; Chauvet, S.-P.; Boullanger, P.; Blum, L. J.; Girard-Egrot, A. P. New Functional Proteo-Glycolipidic Molecular Assembly for Biocatalysis Analysis of an Immobilized Enzyme in a Biomimetic Nanostructure. *Langmuir* **2003**, *19*, 5448–5456.
- (17) Decher, G.; Hong, J. D.; Schmitt, J. Buildup of Ultrathin Multilayer Films by a Self-Assembly Process: III. Consecutively Alternating Adsorption of Anionic and Cationic Polyelectrolytes on Charged Surfaces. *Thin Solid Films* **1992**, *210–211*, 831–835.
- (18) Gurard-Levin, Z. A.; Mrksich, M. Combining Self-Assembled Monolayers and Mass Spectrometry for Applications in Biochips. *Annu. Rev. Anal. Chem.* **2008**, *1*, 767–800.
- (19) National Cancer Institute, <http://www.cancer.gov/cancertopics/factsheet/Detection/tumor-markers> (accessed on Dec. 13, 2014).
- (20) Chen, Y.-S.; Wu, C.-C.; Tsai, J.-J.; Wang, G.-J. Electrochemical Impedimetric Biosensor Based on a Nanostructured Polycarbonate Substrate. *Int. J. Nanomed.* **2012**, *7*, 133–140.
- (21) Rasooly, A.; Jacobson, J. Development of Biosensors for Cancer Clinical Testing. *Biosens. Bioelectron.* **2006**, *21*, 1851–1858.
- (22) Abdi, H.; Williams, L. J. Principal Component Analysis. *Wiley Interdiscip. Rev.: Comput. Stat.* **2010**, *2*, 433–459.
- (23) Ron, H.; Matlis, S.; Rubinstein, I. Self-Assembled Monolayers on Oxidized Metals. 2. Gold Surface Oxidative Pretreatment, Monolayer Properties, and Depression Formation. *Langmuir* **1998**, *14*, 1116–1121.
- (24) Owens, D. K.; Wendt, R. C. Estimation of the Surface Free Energy of Polymers. *J. Appl. Polym. Sci.* **1969**, *13*, 1741–1747.
- (25) Paulovich, F. V. Information Visualization Techniques for Sensing and Biosensing, <http://www.icmc.usp.br/~paulovic/pexensors/> (accessed on Nov. 19, 2014).
- (26) Paulovich, F. V.; Moraes, M. L.; Maki, R. M.; Ferreira, M.; Oliveira, O. N., Jr.; Oliveira, M. C. F. Information Visualization Techniques for Sensing and Biosensing. *Analyst* **2011**, *136*, 1344–1350.
- (27) Moraes, M. L.; Petri, L.; Oliveira, V.; Olivati, C. A.; Oliveira, M. C. F.; Paulovich, F. V.; Oliveira, O. N., Jr.; Ferreira, M. Detection of Glucose and Triglycerides Using Information Visualization Methods to Process Impedance Spectroscopy Data. *Sens. Actuators, B* **2012**, *166–167*, 231–238.
- (28) Ekins, R. P. Ligand Assays: From Electrophoresis to Miniaturized Microarrays. *Clin. Chem.* **1998**, *44*, 2015–2030.
- (29) Oliveira, R. M.; Ferreira, J.; Santos, M. J. L.; Faria, R. M.; Oliveira, O. N., Jr. Probing the Functionalization of Gold Surfaces and Protein Adsorption by PM-IRRAS. *ChemPhysChem* **2011**, *12*, 1736–1740.
- (30) Bhuvana, M.; Dharuman, V. Tethering of Spherical DOTAP Liposome Gold Nanoparticles on Cysteamine Monolayer for Sensitive Label Free Electrochemical Detection of DNA and Transfection. *Analyst* **2014**, *139*, 2467–2475.

(31) Thuo, M. M.; Reus, W. F.; Nijhuis, C. A.; Barber, J. R.; Kim, C.; Schulz, M. D.; Whitesides, G. M. Odd–Even Effects in Charge Transport Across Self-Assembled Monolayers. *J. Am. Chem. Soc.* **2011**, *133*, 2962–2975.

(32) Kuang, R.; Kuang, X.; Pan, S.; Zheng, X.; Duan, J.; Duan, Y. Synthesis of Cysteamine-Coated CdTe Quantum Dots for the Detection of Bisphenol A. *Microchim. Acta* **2010**, *169*, 109–115.

(33) Lapin, N. A.; Chabal, Y. J. Infrared Characterization of Biotinylated Silicon Oxide Surfaces, Surface Stability, and Specific Attachment of Streptavidin. *J. Phys. Chem. B* **2009**, *113*, 8776–8783.

(34) Gonzalez, M.; Bagatolli, L. A.; Echabe, I.; Arrondo, J. L. R.; Argarana, C. E.; Cantor, C. R.; Fidelio, G. D. Interaction of Biotin with Streptavidin: Thermostability and Conformational Changes Upon Binding. *J. Biol. Chem.* **1997**, *272*, 11288–11294.

(35) Colthup, N. B.; Daly, L. H.; Wiberly, S. E. *Introduction to Infrared and Raman Spectroscopy*, 3rd ed.; Academic Press: New York, 1990.

(36) Taylor, D. M.; Macdonald, A. G. AC Admittance of the Metal/Insulator/Electrolyte Interface. *J. Phys. D: Appl. Phys.* **1987**, *20*, 1277–1283.

(37) Oliveira, N. O., Jr.; Pavinatto, F. J.; Constantino, C. J. L.; Paulovich, F. V.; Oliveira, M. C. F. Information Visualization to Enhance Sensitivity and Selectivity in Biosensing. *Biointerphases* **2012**, *7*, 1–15.

(38) Loo, L.; Capobianco, J. A.; Wu, W.; Gao, X. T.; Shih, W. Y.; Shih, W. H.; Pourrezaei, K.; Robinson, M. K.; Adams, G. P. Highly Sensitive Detection of HER2 Extracellular Domain in the Serum of Breast Cancer Patients by Piezoelectric Microcantilevers. *Anal. Chem.* **2011**, *83*, 3392–3397.